Tunable Flux qubits for coupling with spins

May 4, 2015

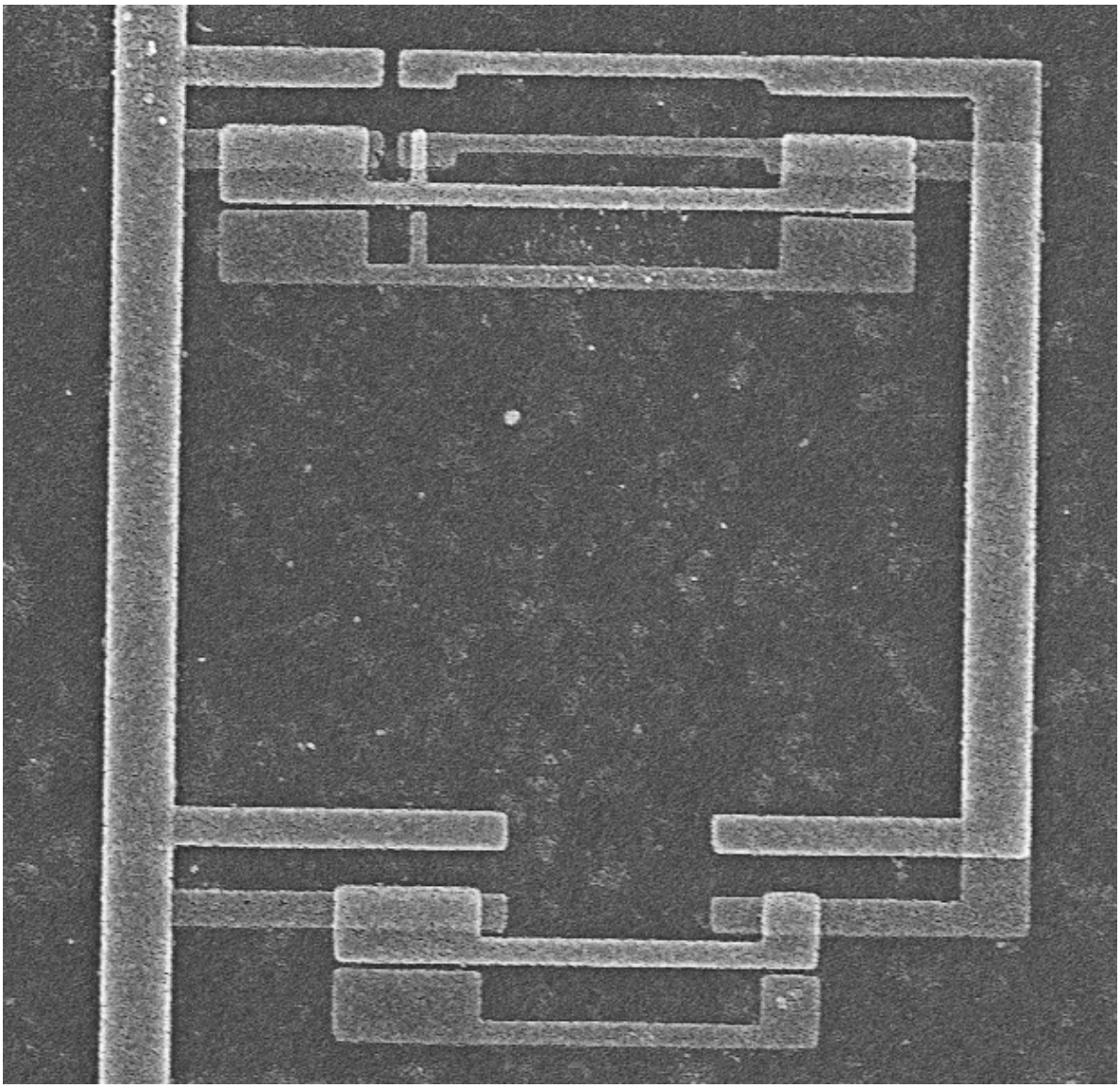

Student: Tikai Chang (parcours ICFP Quantum Physics)
Tutor: Michael Stern
04/05/2015

Foreword

For this internship, I had the pleasure of working in the Quantronics Group at CEA Saclay together with another classmate, Timothée de Guillebon. We were supervised together by Michael Stern and Patrice Bertet in the framework of their ongoing collaboration in the field of flux qubits. Timothée will continue to do a Phd thesis with Patrice Bertet at Saclay, while I will continue onward and do my Phd with Michael Stern at Bar Ilan University in Israel.

Contents

1 Introduction **2**

2 Theoretical description of a flux qubit **4**
- 2.1 Reminders on the Current-Phase Relation of a Josephson junction 4
- 2.2 The potential energy landscape of flux qubit 5
- 2.3 Full simulation 6
- 2.4 The physics near the optimal point of a flux qubit 8
- 2.5 Usage of SQUIDs as tunable junctions 8

3 The experimental setup **10**
- 3.1 3D cavity 10
- 3.2 Coplanar waveguide 11
- 3.3 Fridge and low-temperature measurement 14

4 Fabrication techniques and its characterization **15**
- 4.1 Process overview 15
- 4.2 Post fabrication observations 15

5 Measurement in the dilution fridge **15**
- 5.1 What we seek 15
- 5.2 VNA scan of the resonator line 17
- 5.3 Qubit spectroscopy 17
- 5.4 Rabi Oscillations and Decoherence 19

6 Conclusion and perspectives **21**

1 Introduction

Since the discovery of the first quantum algorithms, quantum computers have triggered intense interest. In theory, these computers could perform much faster calculations than traditional computers for certain computationally demanding problems like factorizing large integers into prime numbers[23] or searching in databases[10]. These unique features have lead scientists and engineers to imagine building quantum processors based on various possible physical realization.

The construction of a quantum computer is extremely difficult due to the extreme fragility of the quantum information. Quantum bits (qubits) must at the same time be strongly inter-coupled by gates to perform quantum computation and well decoupled from the external environment to keep coherence and allow error correction[8].

Spins in semiconductors such as nitrogen vacancy (NV) centers in diamond or phosphorus impurities in silicon can reach very long coherence times [1, 16]- of the order of seconds - and are therefore promising candidates for quantum information processing [11]. The major challenge for an operational quantum processor architecture based on spin-qubits is the realization of gates between distant individual spins. Indeed, a standalone qubit is as useful as a standalone telephone. Recently, a heroic experiment by Bernien et al[22] has demonstrated entanglement of distant NV centers by measuring their emitted optical photons. However, this experiment was extremely complex and the achieved rate of successful entanglement rather low (around one each 10 minutes).

Superconducting qubits are a radically different experimental approach towards the realization of a quantum processor. These qubits consist of macroscopic superconducting circuit elements like capacitors or inductors, connected by one or several Josephson junctions[7]. They have an intrinsic large electromagnetic cross-section and can therefore be easily addressed and coupled together. However, this leads also to a high sensitivity to environmental noise which limits their coherence times compared to spin qubits.

A promising research direction is to combine these two different systems and build an hybrid quantum system that would inherit the advantages and hopefully not the disadvantages of each one of the different components [26]. Indeed, spins in semiconductors with their long coherence time are perfect system to store reliably the quantum information while superconducting qubits with their strong coupling with external fields are perfect systems to process easily fast quantum gates.

This approach requires to transfer efficiently the quantum information between these two systems. One needs to reach the strong coupling regime between the two systems, a regime where the coupling constant is much stronger than the decoherence rate of both systems. Up to now, this has been observed for a superconducting circuit coupled to a spin ensemble only [14]. The long term goal of this work is to reach the strong coupling regime between a single spin and a superconducting circuit.

The feasibility of a hybrid circuit

Let's first estimate the coupling constant g between a single spin and a superconducting circuit. We write the interaction Hamiltonian in the Jaynes Cummings form:

$$H_{int} = -M.\delta B_0 = \hbar g \left(a + a^\dagger\right)\left(\sigma^+ + \sigma^-\right)$$

, where M is the magnetic dipole moment of the spin (roughly one Bohr magneton μ_B), a and $a^\dagger$ are the annihilation and creation operators of a photon in the superconducting circuit, $\sigma^\pm$ are the raising and lowering operator of the spin, and where δB_0 are the vacuum fluctuations of the magnetic field. Assuming that an infinitely thin superconducting line is placed at a distance r from the spin, we get that the coupling constant is given by

$$\frac{g}{2\pi} \approx \frac{\mu_0 \mu_B}{h\sqrt{2}} \frac{\delta I_0}{2\pi r} = 4\,\mathrm{Hz} \frac{\delta I_0\,[\mathrm{nA}]}{r\,[\mu\mathrm{m}]} \tag{1}$$

where δI_0 is the quantum fluctuation of the current in the circuit.

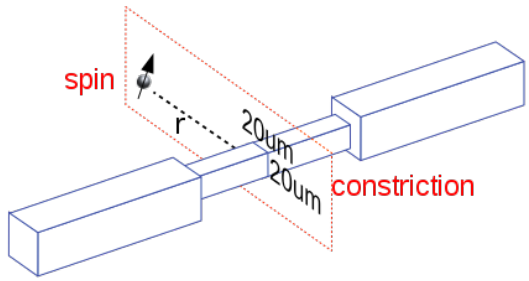

The vacuum current fluctuations in a linear LC resonator are given by

$$\delta I_0 = \omega_0 \sqrt{\frac{\hbar}{2Z_0}} \tag{2}$$

where $Z_0 \equiv \sqrt{\frac{L}{C}}$ is the characteristic impedance and $\omega_0 = \frac{1}{\sqrt{LC}}$. For a typical resonator around 3 GHz with a characteristic impedance of $Z_0 = 50\,\Omega$, this gives 20 nA.

From equation (1), we see the need to reduce r as much as possible. With e-beam lithography, we could build a constriction of cross-section $20\,\text{nm} \times 20\,\text{nm}$. By ion implantation, we could position the spin at a distance of $r \approx 15\,\text{nm}$ from the surface of the constriction. But this would still not be sufficient to reach the strong coupling limit, bringing us at best only up to the kHz range. The only way to increase the coupling is to increase δI_0 in the superconducting circuit. To go beyond the limit set in equation (2), we need a highly non-linear system with large vacuum fluctuations [15, 25]. The flux qubit(flux qubit) is an ideal system for this, with δI_0 up to µA, which could lead to a coupling up to 250 kHz. This is the reason why we chose to work with flux qubits in this internship.

2 Theoretical description of a flux qubit

2.1 Reminders on the Current-Phase Relation of a Josephson junction

Let us start by recalling the two equations governing an S-I-S[1] Josephson junction connecting two superconducting islands 1, 2.

$$\begin{aligned} I &= I_{1\to 2} = I_0 \sin(\varphi_2 - \varphi_1) \\ V &= V_2 - V_1 = \frac{\Phi_0}{2\pi}\frac{d}{dt}(\varphi_2 - \varphi_1) \end{aligned}$$

where φ_i is the phase of the superconducting order parameter of island i, Φ_0 is the magnetic flux quantum, and I_0 the critical current of the junction. The first non linear equation is called the Current-Phase Relation. In the following we note $\varphi = \varphi_2 - \varphi_1$. The potential energy of the junction can be deduced from these two equations.

$$E = \int_{-\infty}^{t} P dt' = \int_{-\infty}^{t} IV dt = -E_J \cos\varphi$$

[1] superconductor-insulator-superconductor

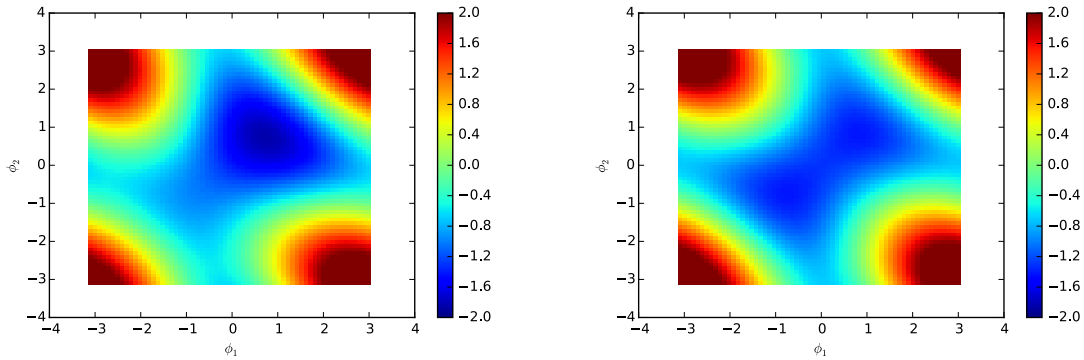

Figure 1: Potential energy landscape of a 3-island flux qubit with parameters $\alpha = 0.7$. Left: $f = 0.4$; Right: $f = 0.5$. We show only one period of φ_i only.

where the Josephson energy is defined as $E_J \equiv I_0 \frac{\Phi_0}{2\pi}$. We also define $\varphi_0 = \Phi_0/2\pi$

2.2 The potential energy landscape of flux qubit

The flux qubit consists of a superconducting loop intersected by three (or more) Josephson junctions[17, 5, 2, 24], among which one of the junctions is smaller than the others by a factor α. It is more convenient experimentally to implement a 4-island loop, but in the following we will discuss only the case of 3-island loops, which captures fully the essence of a flux qubit while keeping simplicity.

The total potential energy of a 3-island-loop writes

$$U = -E_J \cos\varphi_1 - E_J \cos\varphi_2 - \alpha E_J \cos\varphi_3$$

A loop condition on the phase appears due to the Aharonov–Bohm effect when we apply a DC magnetic flux Φ in the loop. The total potential energy of the system transforms to:

$$U = -E_J \left(\cos\varphi_1 + \cos\varphi_2 + \alpha \cos\left(2\pi \frac{\Phi}{\Phi_0} - \varphi_1 - \varphi_2 \right) \right)$$

U is Φ_0-periodic function of Φ, and a 2π-periodic function of $\varphi_1$and φ_2 respectively.

We show on figure 1 that when$\Phi = 0.5\Phi_0 \mod \Phi_0$, two distinct local minima connected by a saddle point appear. The positions of these minima are given by partial derivation $\partial_{\varphi_i} U = 0$. With the φ_i playing identical roles, we can safely suppose that they are identical. $\sin\varphi^\star = \alpha \sin(2\varphi^\star)$ is a sufficient condition to local minimality. In the case of a 3-island flux qubit, we get $1 = 2\alpha\cos\varphi$ and thus $\sin\varphi^\star = \pm\sqrt{1 - \frac{1}{4\alpha^2}}$. [2] We can attribute a physical meaning to the two minima in the potential landscape. They correspond to two different directions of a persistent current I_p flowing in the circuit and given by $I_p = I_0 \sin\varphi^\star$, or

$$I_p = I_0 \sqrt{1 - \frac{1}{4\alpha^2}} \tag{3}$$

[2]For the 4-island flux qubit, a similar derivation gives $\sin\varphi = \pm\sqrt{\frac{3}{4} - \frac{1}{4\alpha}}$

On the line $\varphi_1 = \varphi_2$, this is a superconducting version of the connected quantum 2-well whose generalized position coordinates are the phase differences across junctions. The Heisenberg uncertainty relation between conjugate variables phase and charge $[\varphi_i, n_i] = \mathbf{i}$ ([7]).(where n_j is the number of Cooper pairs having crossed a junction) gives rise to a splitting of the levels Δ(angular velocity) due to the tunneling across the potential barrier. This tunneling element is usually called the *flux qubit gap*.

As seen in the introduction, we seek the largest possible vacuum current fluctuations in our circuit, that is large values of I_p. As shown in equation (3), this leads us to design large junctions with high critical current. However, increasing the critical current of the junctions will give rise to large uncertainties of the flux qubit gap.

This can be seen by deriving the tunneling rate in the W.K.B approximation[17], where the tunneling rate is proportional to

$$t \propto \exp\left(-\frac{\int_{-\varphi^*}^{\varphi^*} \sqrt{2m_{eff}\left(U\left(\varphi\right) - U\left(\varphi^\star\right)\right)}d\varphi}{\hbar}\right)$$

with $m_{eff} = \left(\frac{\Phi_0}{2\pi}\right)^2 2C\left(1+2\alpha\right)$, where C is the capacitance across the junctions[3]. We get in this approximation

$$\Delta \propto \frac{1}{t} \propto \exp\left[-\left(\sin\varphi^\star - \frac{\varphi^\star}{2\alpha}\right)\sqrt{4\alpha\left(1+2\alpha\right)\frac{E_J}{E_C}}\right] \tag{4}$$

where $E_C = \frac{e^2}{2C}$. Increasing the size of the junctions will therefore increase the sensitivity of the gap with respect to α. As is shown in figure 2.

2.3 Full simulation

To produce a more precise estimation of the gap, we need to perform a full simulation taking into account the full Hamiltonian of the system. The Hamiltonian is obtained[6] by performing a Legendre transformation on the Lagrangian $\mathcal{L} = T - U$, where $T = \sum_{i=1}^{3} \frac{Q_i^2}{2C_i}$ is the electrostatic charging energy of the islands, Q_i and C_i being the charge and the capacitance of the i-th island. We get

$$H = 4E_C\left[\frac{1+\alpha}{1+2\alpha}n_1 + \frac{1+\alpha}{1+2\alpha}n_2 - \frac{2\alpha}{1+2\alpha}n_1 n_2\right] + U$$

We diagonalize the Hamiltonian in the charge basis. The $\cos\varphi_i$ terms transform into:

$$cos\varphi_i = \frac{1}{2}\left(\sum_n |n_i\rangle\langle n_i+1| + h.c.\right)$$

[4]From this expression it is then possible to write the reduced[5] Hamiltonian matrix in the charge basis and resolve the eigenenergies numerically. Simulating a 3-island qubit instead of a 4-island flux qubit is therefore much lighter due to the dimensionality of the subspace.

[3]any one of the two non α junctions

[4]Using the fact that $\langle n|\exp\left(i\varphi\right)|n'\rangle = \int\langle n|\varphi\rangle\exp\left(i\varphi\right)\langle\varphi|n'\rangle = \delta_{n'+1,n}$

[5]in a computer simulation we are obliged to truncate to a finite number of charge states

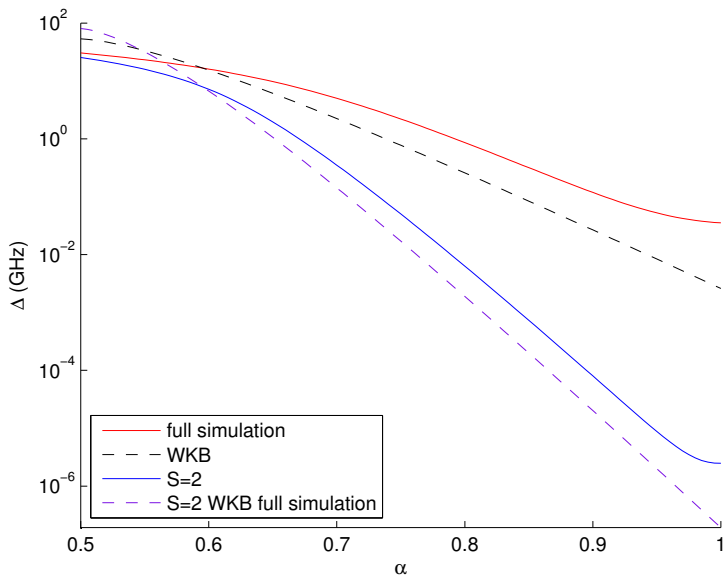

Figure 2: The qubit gap as a function of α and surface S of the big junctions such that $E_J = S \times 350\,\text{GHz}$ and $E_C = \frac{1}{S} \times 5\,\text{GHz}$. We see that the logarithmic dependence on α fits well with the WKB approximation for non-pathological α's ($\alpha > 0.5$).

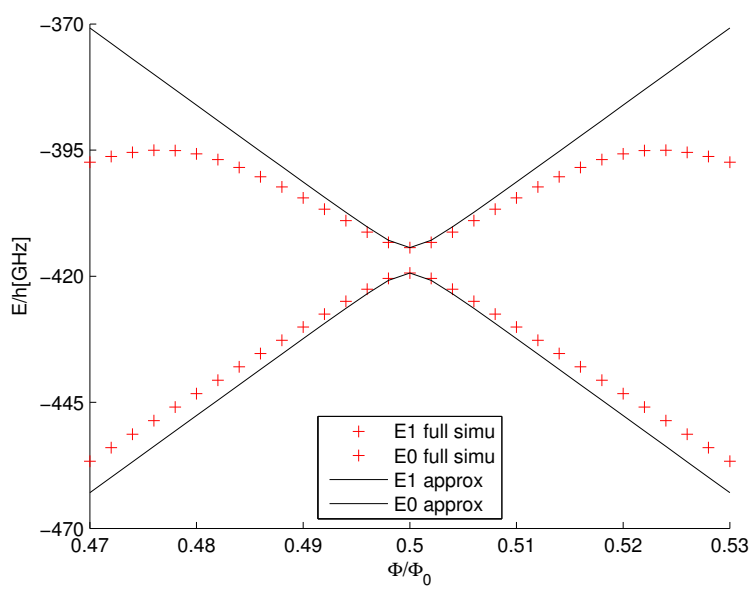

Figure 3: Simulation of the qubit levels as a function of the magnetic frustration $\frac{\Phi}{\Phi_0}$, compared with the approximative Hamiltonian of equation (5). .

2.4 The physics near the optimal point of a flux qubit

Close to the *optimal point* ($\Phi = 0.5\Phi_0\,[\Phi_0]$), a simplified version of the Hamiltonian arises naturally from the W.K.B. tunneling framework. It writes in the current basis

$$H = \frac{\hbar}{2}\left(\varepsilon\sigma_z - \Delta\sigma_x\right) \tag{5}$$

where $\varepsilon = \frac{2I_p}{\hbar}\left(\Phi - 0.5\Phi_0\right)$ Δ is the gap[6] of the qubit, and the σ's are Pauli matrices. The difference between the two eigenenergies is

$$\hbar\omega_{01} = \hbar\sqrt{\Delta^2 + \varepsilon^2} \tag{6}$$

We compare the approximation to the full simulation in figure 3 and see excellent agreement close to the optimal point. It is important to note that the dependence of ω_{01} as a function of Φ is huge. $\frac{\varepsilon}{2\pi}$ can increase by up to $1 - 3\,\mathrm{GHz}m\Phi_0^{-1}$, and therefore even a limited flux noise leads to rather bad coherence times of the qubit. The only point where we can expect to have longer coherence times is at the so-called *optimal* point, precisely at $\Phi = \frac{\Phi_0}{2}$, where the flux qubit is immune to flux noise thanks to the zero-derivative with respect to Φ.

2.5 Usage of SQUIDs as tunable junctions

In the perspective of coupling a flux qubit to a spin at the optimal point, we need therefore to tune the gap of the flux qubit to the spin resonance. At the same time, we need to increase as much as possible the persistent current of the flux qubit to increase the coupling g (equation (1)). This means increasing the critical current of the junctions I_0 (equation (3)) and therefore E_J. However, we have seen previously in equation (4) that increasing the critical current of the junction will lead to unpredictable values of the gap Δ.

We need therefore a way to tune the gap of the qubit. To do this, we can replace one of the junctions by a symmetric SQUID which consists of two identical junctions placed in parallel[18]. The symmetric SQUID behaves as a tunable Josephson junction whose Josephson energy is given by $E_J \cos 2\pi\frac{\Phi_S}{\Phi_0}$ [20], where Φ_S is the flux threading the loop of the SQUID. In figure 4, we show that indeed this allows to tune the gap of the flux qubit. However, the reported decoherence rates Γ_φ of flux qubits in Ref. [18] were shown to be large even at the optimal point ($\Gamma_\varphi \gg 1\,\mathrm{MHz}$). We believe that the origin of this is due to the flux noise $\delta\Phi_0$ which affects the SQUID and therefore the gap value.

It can be shown that in the case of a 1/f noise, $\Gamma_{\varphi R} \approx 3.7\,|\partial_{\Phi_S}\Delta|\,|\delta\Phi_0|$ [13]. In this internship, we tried to circumvent this problem by using asymmetrical SQUIDS where we expect a smaller value of $|\partial_{\Phi_S}\Delta|$. In an asymmetric SQUID, the Josephson energies of the two junctions $E_{J_{1/2}}$ are such that $E_{J_{1/2}} = E_J\frac{1\pm d}{2}$, with $d \in]0,1[$ (see figure below).

[6] defined previously on page 6. Do not confuse it with the difference between the two levels ω_{01}. They agree only at the optimal point

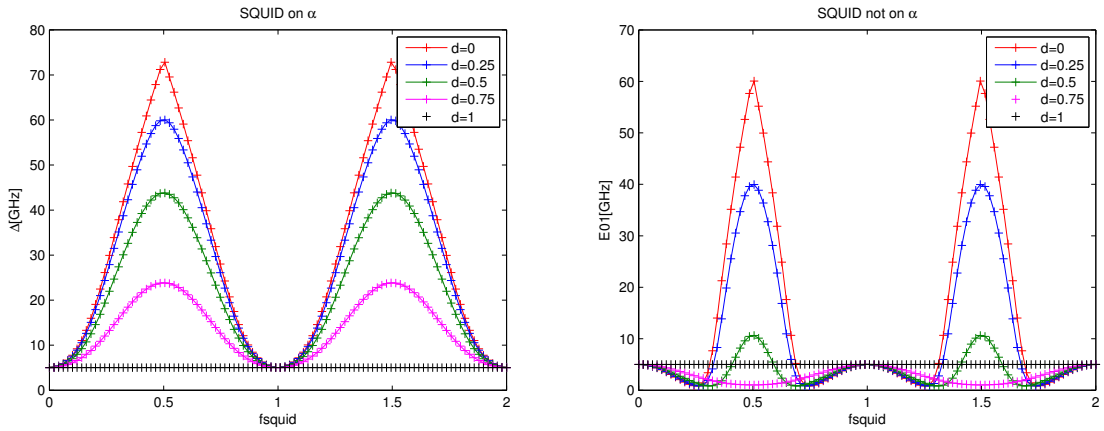

Figure 4: The gap dependence is different whether the SQUID replaces the α-junction or the one of the big junctions. Replacing the α-junction by an assymmetric SQUID increases the value of the gap while replacing one of the big junctions decreases its value. In both cases, the dependence of Δ vs Φ_S decreases with d.

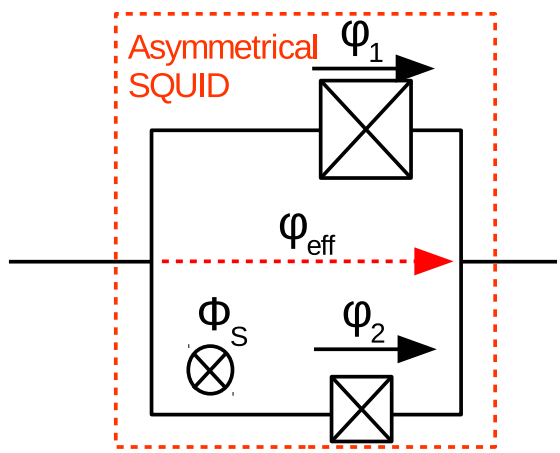

The energy of this system writes:

$$\begin{aligned} U_S &= -E_{J_1}\cos\varphi_1 - E_{J_2}\cos\varphi_2 \\ &= -E_J\sqrt{\cos^2 2\pi\frac{\Phi_S}{\Phi_0} + d^2\sin^2 2\pi\frac{\Phi_S}{\Phi_0}}\cos\left(\varphi_{eff} + \arctan\left(d\tan 2\pi\frac{\Phi_S}{\Phi_0}\right)\right) \end{aligned} \tag{7}$$

Therefore the effective Josephson energy of the SQUID is now $E_J\sqrt{d^2 + (1-d^2)\cos^2 2\pi\frac{\Phi_S}{\Phi_0}}$ and is thus less sensitive to the flux threading the loop of the SQUID compared to the symmetric case. We therefore expect that a flux qubit embedding an asymmetrical SQUID would have better coherence times. In this internship, we designed the asymmetric parameter $d \approx 0.8$ such that $T_\varphi = \frac{1}{\Gamma_\varphi} > 10\,\mu\text{s}$. [7]

[7] We note that the additional phase in equation (7) introduces a shift of the optimal point of the main loop.

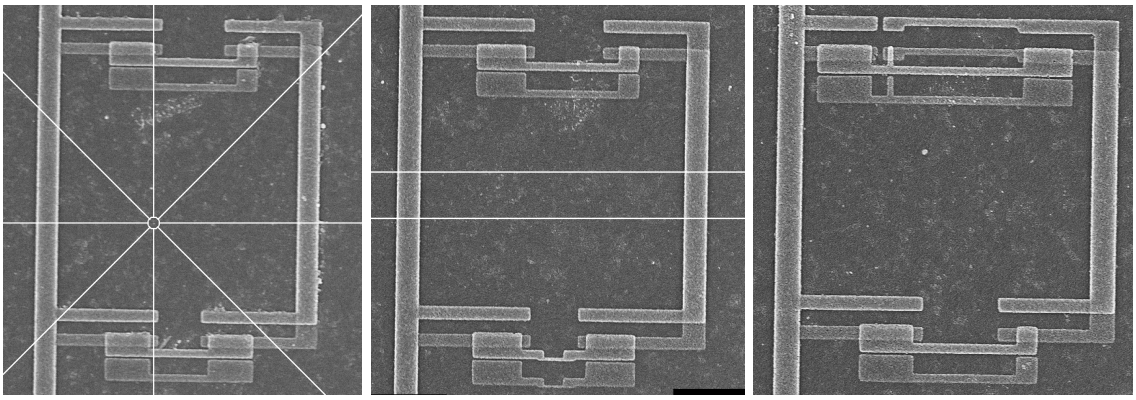

Figure 5: In reading order: flux qubit with big junctions, flux qubit with constriction, flux qubit with SQUID

3 The experimental setup

A first method for flux qubit readout consists in measuring a SQUID placed in the close vicinity of a flux qubit. The persistent current of the flux qubit modifies the flux threading the SQUID, and hence the inductance of the readout circuit [4, 5, 2]. In this internship, we follow a different path. We couple the flux qubit to a resonator, and readout the state of the qubit by measuring the dispersive shift of the resonator[3]. This can be done with a *two dimensional resonator* which takes the form of a coplanar waveguide, or with a *three dimensional resonator* which consists of a 3D metallic cavity. Coplanar waveguide designs are better suited for placing multiple DC/AC magnetic flux lines to control the qubits while 3D cavities are less convenient but increase by up to an order of magnitude the qubit lifetimes[19] thanks to a better control of the electromagnetic environment.

3.1 3D cavity

A 3D cavity setup was already in place at the start of the internship[24]. This cavity is made of copper to allow the application of an external magnetic field and tune the flux threading the qubit around $\Phi_0/2$. The cavity dimensions are such that the first mode of the cavity is around 5GHz. Indeed, the frequency of this mode is given by

$$f_0 = f_{1,0,0} = c\sqrt{\frac{1}{L^2} + \frac{0}{W^2} + \frac{0}{H^2}}$$

where $L > W > H$ are the dimensions of the 3D box. We find that the dimensions of the cavity are of the order of a few tens of millimeters ($72\,\mathrm{mm} \times 30\,\mathrm{mm} \times 5\,\mathrm{mm}$). The quality factor of the first mode of the cavity is chosen to be around $Q_{cav} \approx 500$, well below the internal losses $Q_{in} \sim 10000$, and is fixed by the penetration length of the antennas shown in figure 6.

The direct coupling between the cavity and a micron-sized flux qubit is given by $\frac{(I_p \times A) \times \delta B_0}{\hbar} = I_p A \sqrt{\frac{\mu_0 \omega_0}{2\hbar(LWH)}} \approx 30\,\mathrm{kHz}$, where δB_0 is the quantum fluctuation of the magnetic field in the cavity ($\frac{\delta B_0^2}{2\mu_0}(LWH) = \frac{\hbar\omega_0}{4}$), and A is the area of the flux qubit. Clearly, this is insufficient.

We thus use a lumped-element LC resonator as a intermediate resonator that is coupled inductively to the flux qubit and capacitively to the first mode of the 3D cavity. The coupling

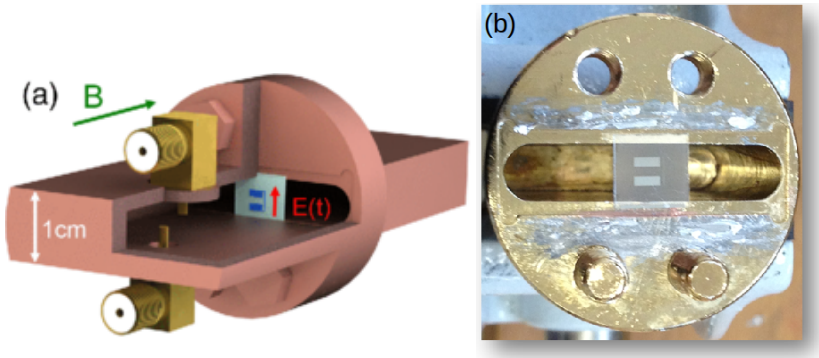

Figure 6: (a) Cutaway representation of the 3D cavity, with the LC circuit (in blue) on its sapphire chip. The green arrow represents the applied magnetic field B. The red arrow represents the ac electric field E(t) of the first mode of the cavity. Schematic diagram of the 3D cavity. we show two antennas coupling the cavity to the exterior. (b) Photo of the cross section of the cavity.

between the LC resonator and the cavity can be estimated by $g_{res} \sim \frac{\delta E_0 (d \times e)}{\hbar}$ where δE_0 is the quantum fluctuation of the electric field in the cavity ($\frac{\epsilon_0 \delta E_0^2}{2}(LWH) = \frac{\hbar\omega_0}{4}$), d being the length of the LC resonator. It can reach up to 100 MHz for $d = 3$ mm. In a first approximation, the quality factor of the LC mode can be estimated by the Purcell formula $Q_{res} = Q_{cav}\left(\frac{\delta}{g_{res}}\right)^2$ where δ is the detuning between the LC resonator and the first mode of the cavity. For $f_{res} = 4.5$ GHz, $Q_{res} \approx 10000$. Of course the above is only an approximative approach and has to be completed by a proper 3D electromagnetic simulation (CST).

3.2 Coplanar waveguide

The design process of the coplanar waveguide alternates between verification on a EM-simulation software called *Sonnet* and drawing on AutoCAD 2015. In this design the incoming signal will arrive by a coaxial cable soldered on the chip. The impedance of the resonator should therefore be fixed at $Z_0 = 50$ ohms, since a matched impedance will ensure that the signal is fully transmitted into and out of the resonator without giving rise to reflections. The substrate's relative permittivity (for sapphire $\varepsilon_r = 9.3$ or 11.5 depending on the direction) and the thickness of the metallic layer fix the cross section geometry in particular the trace width W and ground plane spacing G, shown in figure 7.

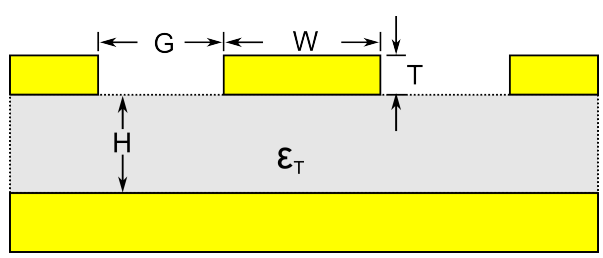

Figure 7: Cross section geometry

The next step is then to design resonator such that the frequency of the first mode is $f_{res} = 5\,\text{GHz}$ and the quality factor is $Q \approx 5000$. To do so, the length the resonator L must verify the resonant condition $\frac{f_{res}L}{2} = \bar{c}$, where $\bar{c} \approx c/\sqrt{\varepsilon_r}$ is the speed of electromagnetic waves in the coplanar wave guide. We obtain $L \approx 12\,\text{mm}$ for our design. Then, in order to set $Q = 5000$, a high impedance element such as an interdigitated capacitor would act as a semi-reflecting mirror in optics. The loss rate associated to one capacitor of capacitance C writes[21]

$$\kappa = \frac{P_{dissi}}{E_{stored}} = \frac{2\omega_{res}Z_0}{\pi}\Re\left(\frac{1}{Z_0 + \frac{1}{iC\omega_{res}}}\right) \approx \frac{2\omega_{res}^3 C^2 Z_0^2}{\pi} \tag{8}$$

The basic design would be to employ a symmetrical design. We would need in this case

$$C_c = \sqrt{\frac{\pi}{2Q}}\frac{1}{Z_0\omega_{res}}$$

Since we are measuring in transmission, a good strategy is to adopt an asymmetrical design in which the coupling capacitor is greater on one side so that a better signal to noise is obtained. We design our cavities such that $\kappa_1 \approx 10\kappa_2$, by using $C_1 = 11\,\text{fF}$ and $C_2 = 4\,\text{fF}$.The precise values of the capacitance of the interdigitated capacitors is obtained by varying the size of the fingers and their distances and by using a 2.5D electromagnetic simulator (Sonnet). See figure 8.

The main interest of a coplanar wave guide is to introduce AC/DC current lines capable of applying a magnetic field individually on each qubit. We must however verify that the Purcell rate of a qubit introduced by the flux lines is not too large. Its expression can be derived from the Fermi Golden Rule $\Gamma_{Purcell}^{FL} = \frac{\pi}{2}S_{\Phi_0/\varphi_0}(\omega_{01})\left|D_{\Phi_0/\varphi_0}\right|^2$, where $D_{\Phi_0/\varphi_0} = 2\pi\left(\partial_\Phi\varepsilon\right) = \frac{2I_p}{\hbar}\varphi_0$ is the transition amplitude between the ground and excited states of the flux qubit due to the perturbation part of the Hamiltonian $\varepsilon\sigma_z$ in equation (5) and where $S_{\Phi/\varphi_0}(\omega)$ is the spectral density of reduced[8] flux $\frac{\Phi}{\varphi_0}$. $S_{\Phi/\varphi_0}(\omega) \approx \left(\frac{M}{\varphi_0}\right)^2\frac{\hbar\omega}{2\pi}\frac{2}{Z}$ in the low temperature limit, with M being the mutual inductance between the flux qubit and the flux line. We get that

$$\Gamma_{Purcell}^{FL} = \frac{4I_p^2M^2}{\hbar Z_0}\omega_{01}$$

The numerical application for $\omega_{01}/2\pi = 5\,\text{GHz}$ gives

$$T_{Purcell}^{FL} = \frac{250\,\mu\text{s}}{\left(M\,[\text{pH}]\right)^2\left(I_p\,[\text{nA}]\right)^2}$$

To have $T_{Purcell}^{FL} = 20\,\mu\text{s}$, we need $M = 0.2\,\text{pH}$ assuming $I_p = 500\,\text{nA}$.

We can approximate $M \approx \mu_0\frac{A}{2\pi r}$, where r is the distance between the flux qubit. The size of the flux qubit being $A = 4\,\mu\text{m} \times 4\,\mu\text{m}$, this fixes the minimal distance between the flux qubit and the flux line. We see clearly the trade-off between decreasing M to increase $T_{Purcell}^{FL}$ and still being able to apply easily several Φ_0's on the flux qubit with a small DC current ($I \leq 10\,\text{mA}$).

During this internship, two variants of the mask were designed (see figure 8). In one version, the flux line is short-circuited to the ground of the chip whereas in the other, the

[8] $\frac{\Phi}{\varphi_0}$ is without units such that $\frac{\Phi}{\varphi_0} = 2\pi$ when $\Phi = \Phi_0$

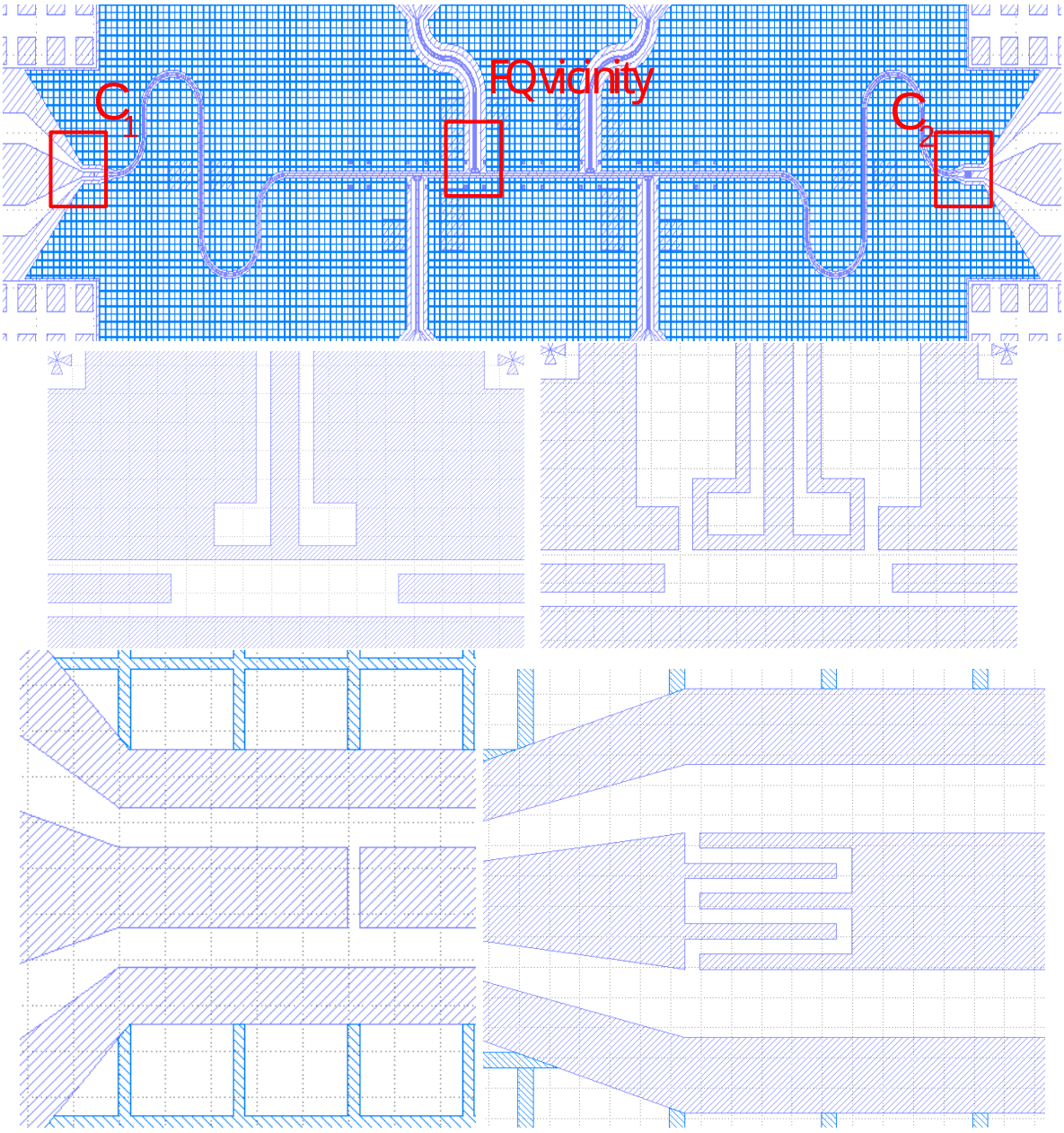

Figure 8: Design and various zooms. Below: asymmetrical capacitive coupling. Top-Mid left and top-mid right: Two versions of how to connect the local flux line to the ground.

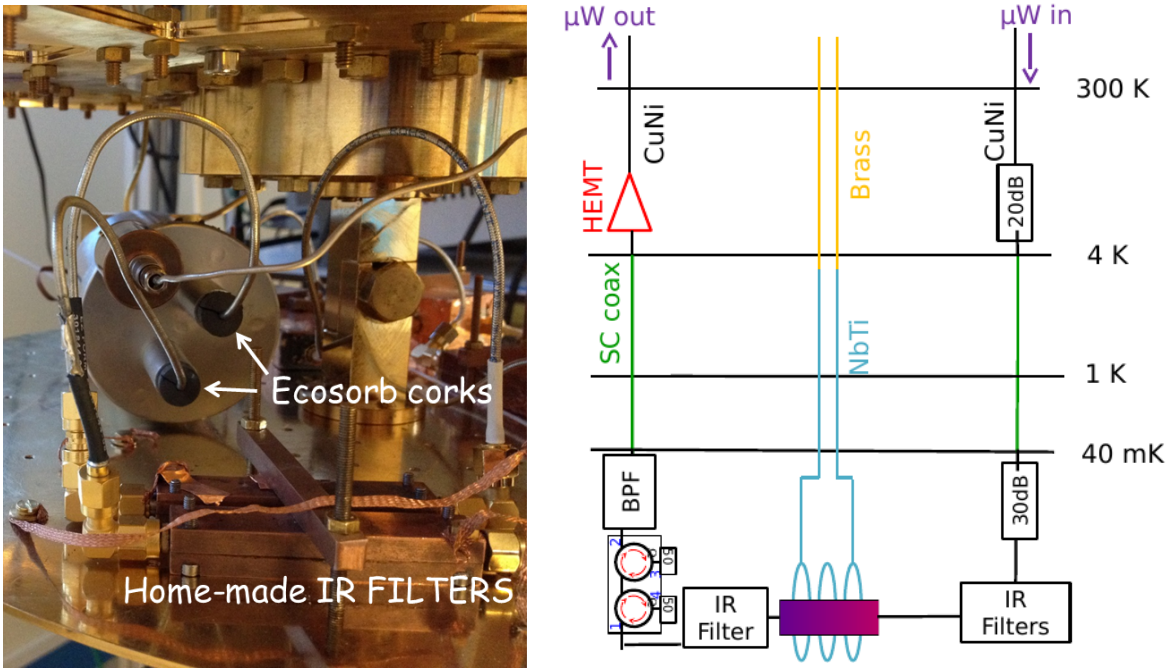

Figure 9: A series of filters and circulators prevents the hot ambient photons from entering the cavity.

flux line has its own ground. In order to trap possible magnetic vortices, the ground of the chip is gridded. To avoid ground loops, we prepared connection pads in the middle of the ground plane to connect the different parts of the ground together. Other connection pads were designed far away from the resonator to enable test junction characterization.

3.3 Fridge and low-temperature measurement

The temperature of the experiment is maintained at around $T = 35\,\mathrm{mK}$ using a dry dilution fridge. Even if the sample is cooled down to such a low temperature, the temperature of the electromagnetic field in the resonator can be substantially different due to incoming photons from room temperature. It is therefore essential to protect the samples from this hot electromagnetic radiation. The number of thermal photons at the resonator frequency coming from outside is approximately $n \approx \frac{k_B T_{ambiant}}{\hbar\omega} = 1000$. And therefore the input signal is strongly attenuated by 20dB at 4 K and 30dB at 20 mK to get to less than one thermal photon in the cavity. For the output signal, circulators (equivalent to an optical diode in the microwave range) are used to allow the signal coming out of the fridge while attenuating strongly the signal in the other direction. In addition to this, home-made low-pass filters are added to filter out any remaining infrared photons (figure 9).

4 Fabrication techniques and its characterization

4.1 Process overview

During my internship I had to fabricate several samples. The fabrication of a sample is comprised of the following steps, as summarized in figure 10:

1. *Wafer preparation and cutting.* The sapphire chip is patterned to form a lumped element LC resonator by optical lithography and aluminum evaporation. The wafer is then covered by a tri-layer coating which consists of 500 nm MAA -50 nm Ge - 120 nm PMMA. The wafer is then cut into samples.

2. *E-beam lithography* By e-beam lithography (E-line Raith, 25 keV) we expose with various doses the interconnections of the LC circuit and the pattern of six flux qubits.

3. *Development and etching.* The PMMA layer is developed in MIBK:IPA(1:3), followed by Reactive Ion Etching (RIE) of the Ge layer using SF_6 ($P = 2\mu$bar, $V = 100$ V, $t \approx 20$ s). This step is followed by oxygen etching which is used to remove an undercut below the Ge mask (In two steps: $P = 4\mu$bar, $V = 125$ V during $t \approx 8$ min followed by $P = 100\mu bar$, $V = 65$ V during $t \approx 60$ min).

4. *Multi-angle evaporation and oxidation.* Aluminum is first evaporated with a 20° angle followed by a dynamical oxidation step ($P = 25\mu$bar,$t = 10$ min). The second layer of aluminum is evaporated with 0° angle to form the junctions.

4.2 Post fabrication observations

It is very important to verify the success of the oxidation step of the junctions before measuring the sample at low temperature since the time for heating and re-cooling the fridge is of the order of magnitude of a day.

The critical current is exponentially dependent on the thickness of the oxide layer in an S-N-S junction. This thickness can vary slightly from sample to sample depending on the precise conditions of the dynamical oxidation. We have seen previously that flux qubit gaps are also exponentially dependent on the critical current of the junctions and it is therefore crucial to control this step.

To estimate the critical current of the junctions at room temperature, we use the Ambegaokar-Baratoff relation, which connects it to the tunnel resistance by:

$$I_0 = \frac{\pi\Delta}{2eR_n}$$

Where Δ is the superconducting gap (200 µeV) and R_n is the tunnel resistance.

5 Measurement in the dilution fridge

5.1 What we seek

In [24], flux qubits were reported to have a persistent current of $I_p \approx 150$ nA and very long lifetimes of $T_2 \approx 10$ µs. We recall that in the view of building hybrid spin-flux qubit systems, we

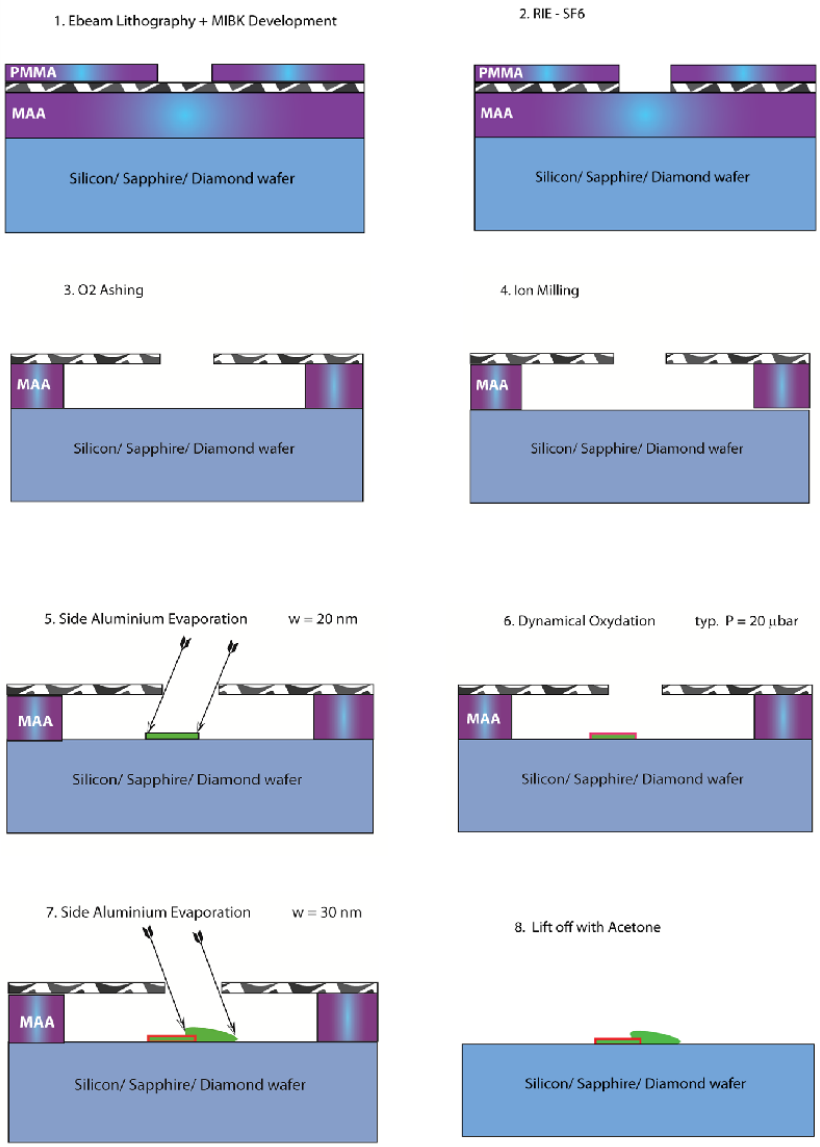

Figure 10: Flow chart of the fabrication process

would need additional modifications to increase the spin-flux qubit coupling, notably adding a constriction and increasing the persistent current (by changing the critical current of the junctions as shown in equation (3)). The fact that we work at the optimal point to have good coherence times means also that fine tuning of the gap using asymmetrical SQUIDs is required. That is why in this internship, we sought to characterize the effects of these various modifications on the flux qubits.

In our sample, we prepared six flux qubits with a much higher critical current ($I_0 \approx 1.5\,\mu\text{A}$ compared to $I_0 \approx 500\,\text{nA}$ in [24]), among which two of them have an asymmetric SQUID junction and two have a 35-nm constriction.

The characterization of these qubits is done by the following steps:

1. Detection of the flux qubits anticrossings/dispersive shifts with a Vector Network Analyser.
2. Spectroscopy of each qubit
3. Rabi oscillations and T_1, T_2 and T_{2echo} measurements

5.2 VNA scan of the resonator line

Qubit detection is done using a Vector Network Analyser (VNA). We measure the transmission amplitude of the LC resonator as a function of the measure frequency f_{meas} and the magnetic field. The VNA is capable of producing a chirping signal and measures in one scan the frequency-dependent scattering coefficients $s_{ij}, (i,j) \in \{1,2\}$. We scan only in a range of a few tens of MHz around the LC resonator frequency to detect the qubits which are manifested by a change in the resonator frequency (measured to be 4.6553 GHz at $B = 0G$). See figure 11.

Anticrossing between the qubit line and the resonator line is a direct indication of the presence of a qubit below the resonator frequency. The amplitude of the anticrossing gives direct access to the coupling constant g of the qubit with the resonator[12]. If the qubit transition frequency does not cross the resonator frequency (in the limit where the detuning is large compared to the coupling) it gives rise to a dispersive shift $\pm\chi \approx \frac{g^2}{|\delta|}$ whose sign depends on the relative position of the two lines.

5.3 Qubit spectroscopy

We use the dispersive shift to make a full spectroscopy of the qubit. Indeed, when applying a pump pulse at precisely the resonance frequency of the qubit, it is possible to put it in its excited state. This change will be manifested by a shift 2χ of the resonator frequency.

Experimentally speaking, we measure the amplitude and phase of the transmitted signal by demodulating the signal using an IQ mixer. The measurement frequency is tuned at the maximum of the signal amplitude when the qubit is in the ground state. When the qubit is excited, a dip is seen in the transmitted amplitude.

In figure 12, we show the spectroscopy of the two flux qubits we measured during the internship. From this spectroscopy, the parameters of the qubits can be fitted, and we get for each qubit, its gap and persistent current. Namely, for qubit A, $\Delta^A = 9.8GHz$, $I_p^A = 470nA$, and for qubit B, $\Delta^B = 1.2\,\text{GHz}$ and $I_p^B = 830\,\text{nA}$. It was difficult to measure a signal for

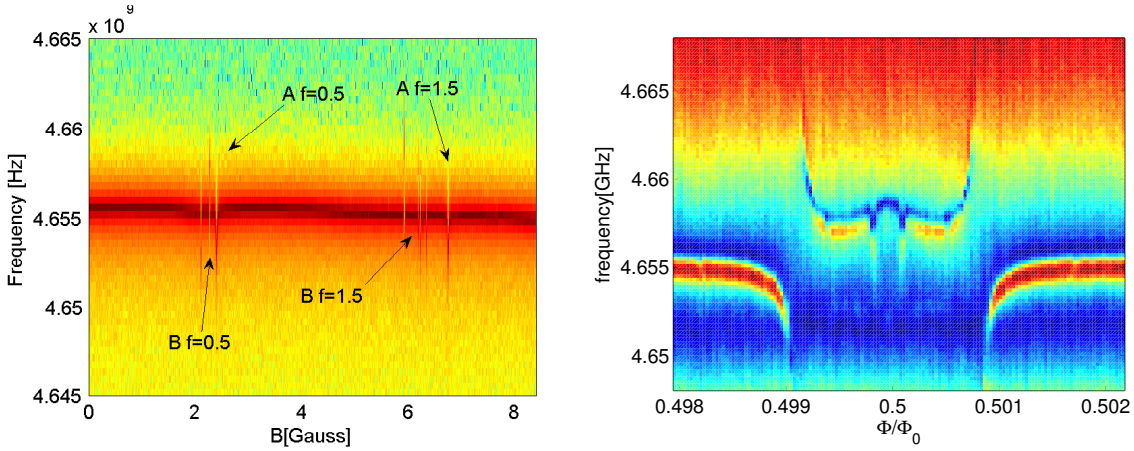

Figure 11: Left: VNA scan versus external applied magnetic field B. The qubits are manifested by an abrupt change of the resonance frequency of the resonator. They appear at different values of magnetic field due to the fact that we designed them with different surfaces so that the flux threading the loop is different for each qubit. Qubit A and B shown in the figure appear twice for magnetic fields which correspond to $\Phi_0/2$ and $3\Phi_0/2$. Right: Zoom of the anticrossing of qubit B in the vicinity of $\Phi_0/2$. Using spectroscopic data in section 5.3 we can fit the coupling constant to be $120MHz$

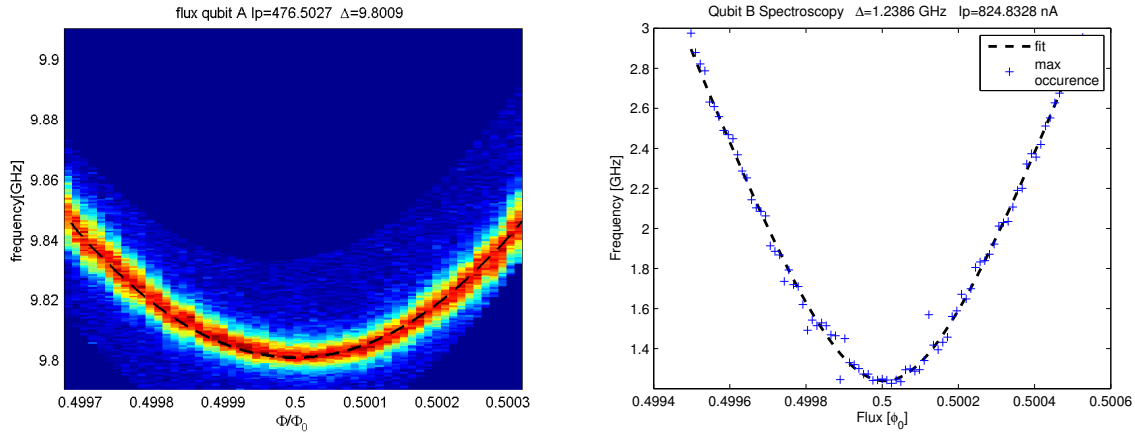

Figure 12: Spectroscopy of the flux qubit A and B. The signal becomes harder to see for qubit B due to its small transition frequency compared to the ambient temperature.

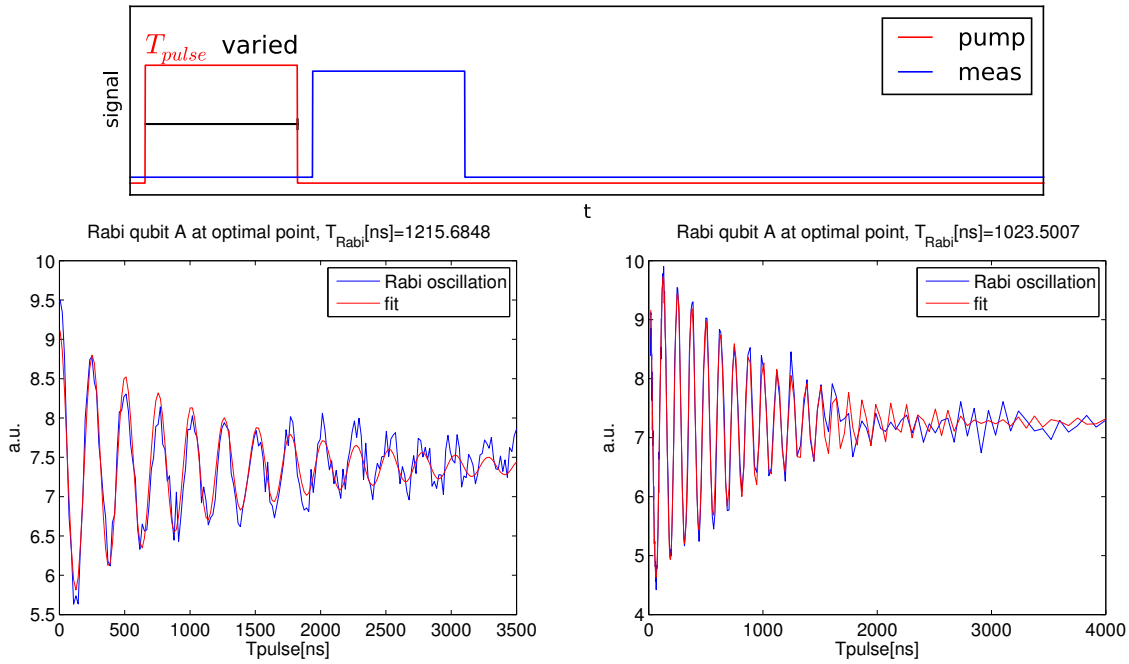

Figure 13: Rabi oscillation sequence and results for flux qubit A. We show the oscillation of the I component with respect to its stationary value. The Rabi decay time is roughly $T_{Rabi} \approx 1000\,\text{ns}$. The plot on the right is obtained by multiplying by four the power and we see that the Rabi frequency is doubled.

qubit B, especially at its optimal point, most likely because it was too hot.[9] We plan to use a dynamical decoupling method called DDROP[9] for resetting the qubit to the ground state. This method, inspired by dynamical cooling of nuclear spins, could enable us to go further for the full characterization of qubit B.

5.4 Rabi Oscillations and Decoherence

Rabi oscillations occur when we apply an external strong microwave drive at the frequency of the qubit. In the absence of decoherence, the probability for a flux qubit to be in the excited state would oscillate periodically *forever* as a function of the length of the pumping pulse. The period of the oscillations is inversely proportional to the applied AC electromagnetic field. In figure 13 we show the Rabi oscillations of qubit A close to its optimal point at different pump powers. The decay of the Rabi oscillations is due to relaxation and decoherence. As we increase the frequency of the oscillations, the effect of low frequency noise is filtered out, increasing therefore the Rabi decay time, up to a theoretical limit of 4/3T1.

The relaxation time T_1 of the qubit is obtained by applying a so-called pi-pulse (see Fig) that put the qubit in tis excited state and looking at how long it takes for the qubit to relax to its ground state. In Fig. We show the the dependency of T_1^A on the magnetic frustration

[9] To be able to detect a qubit using this method, its resonance frequency should be high compared to the temperature of the fridge ($\frac{k_B T_{fridge}}{h} \approx 1\,\text{GHz}$) such that the qubit is initially in its ground state.

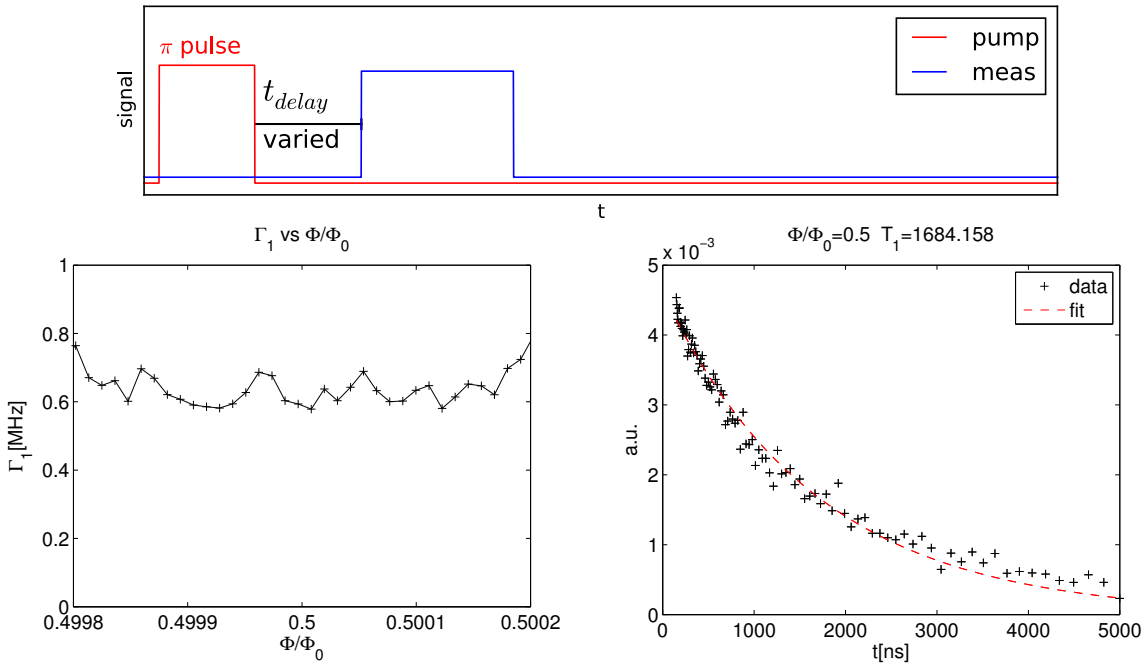

Figure 14: T_1 measurement sequence and results. We show the the dependency of T_1^A on the magnetic frustration of the flux qubit Φ/Φ_0. T_1 is sensibly invariant to the frustration. We also show T_1^A for $\Phi/\Phi_0 = 0.5$. We show on the right the evolution of the signal at the optimal point as a function of T_{delay}.

of the flux qubit Φ/Φ_0, and we extract $T_1^A = 1.5\,\mu\text{s}$ at the optimal point. As expected, T_1 is relatively insensitively to the flux threading the flux qubit in the vicinity of the optimal point.

The Ramsey interferometry can be used to define the coherence time $T_{2Ramsey}$. To see how this works we focus on the decoherence-free case. We first apply a $\pi/2$-pulse rotation to bring the flux qubit from the ground state to a superposition of the ground and excited state $\frac{|0\rangle+i|1\rangle}{\sqrt{2}}$. During some time t, no pulse is applied and the system acquires a phase between the ground and excited state $\frac{|0\rangle+e^{-i\delta t}i|1\rangle}{\sqrt{2}}$ according to the Hamiltonian $\frac{\hbar\delta}{2}\sigma_z$, where $\delta = \omega_{01} - \omega_{pump}$ is the detuning in the rotating wave approximation. A second $\pi/2$-pulse then brings the state to $\frac{(1-e^{-i\delta t})|0\rangle+i(1+e^{-i\delta t})|1\rangle}{2}$. The detection probability of finding the flux qubit in the excited state fluctuates between 0 and 1 at an angular frequency δ.

When decoherence and spontaneous emission is considered, the oscillation amplitude decreases exponentially. We present in figure 15 the Ramsey fringes of qubit A. We chose to detune the pump by $|\delta|/2\pi = 5\,\text{MHz}$.

To filter out low-frequency noise, it is possible to use the Hahn echo method. The sequence consists of two $\pi/2$ pulses[10] sandwiching a π pulse. Since we no longer want to see the Ramsey fringes, we set $\delta_{theorical} = 0$. But δ still fluctuates around zero due to low frequency noise. Starting from the state $\frac{|0\rangle+e^{-i\delta t/2}i|1\rangle}{\sqrt{2}}$ just after the first delay time, the π-pulse inverses the flux

[10] the excitation pulses in this paragraph are all approximated to be instantaneous

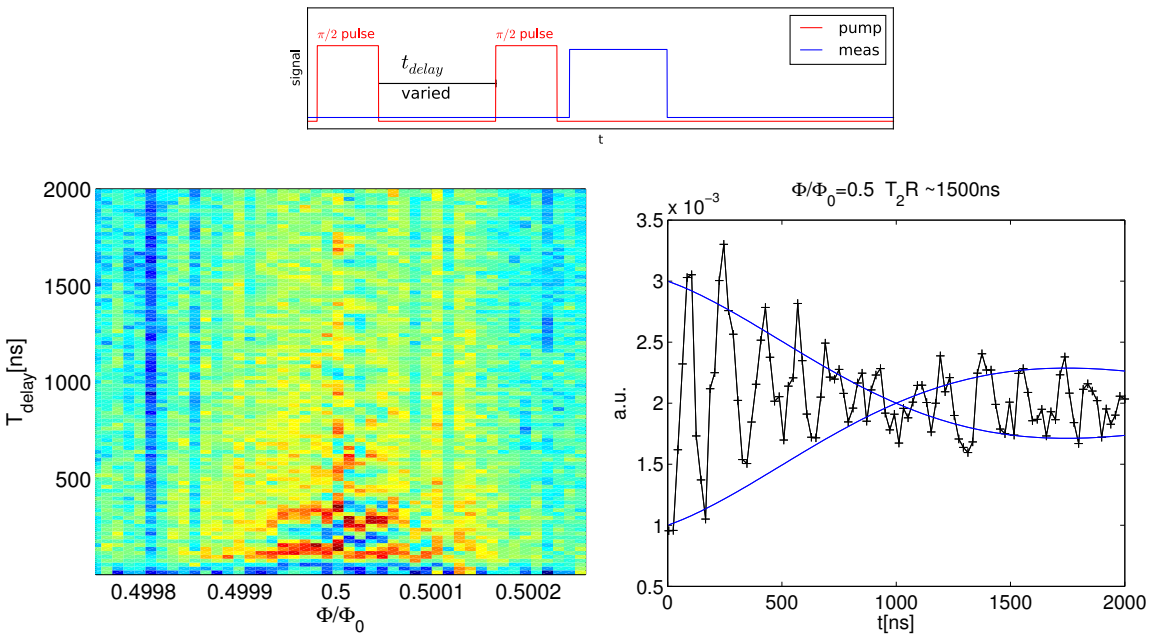

Figure 15: Ramsey measurement sequence and results for flux qubit A. Left: Ramsey fringes. Right: cut at $\frac{\Phi}{\Phi_0} = 0.5$

qubit state to $\frac{i|1\rangle - e^{-i\delta t/2}|0\rangle}{\sqrt{2}}$. At the end of the second delay time, the state is $\frac{e^{-i\delta t/2} i|1\rangle - e^{-i\delta t/2}|0\rangle}{\sqrt{2}}$, which is up to a global factor $\frac{|0\rangle - i|1\rangle}{\sqrt{2}}$. After the last $\pi/2$-pulse, the state returns to the ground state with a global constant. The free evolution of the first delay time cancels out the free evolution of the second delay time insensitively to δ and explains the immunity to low frequency phase noise. The T2 echo measurement of flux qubit A is presented in figure 16.

One can extract the pure dephasing rate by substracting the contribution of the relaxation. It is given by $\Gamma_{\varphi E} = \frac{1}{T_{2E}} - \frac{1}{2T_1}$. This allows us to determine the amount of flux noise in our system by using the formula $\Gamma_{\varphi E} = \sqrt{\ln 2}\,|\delta\Phi_0| \left|\frac{d\omega_{01}}{d\Phi}\right|$[13]. We get $8\mu\Phi_0/\sqrt{Hz}$ at 1 Hz, which is rather high in comparison to [24]. Interestingly, we find a strong deviation from the linear dependence in the vicinity of the optimal point. This could be due to the high current flowing in the loop, which could give rise to second order corrections.

6 Conclusion and perspectives

The internship paves the way for the Phd thesis I will do in Israel, whose long-term goal will be to build hybrid systems coupling strongly to spins using flux qubits. This internship was an opportunity for me to learn the theoretical aspects of the flux qubit as well as its fabrication. Starting from [24], we investigated the effects of adding constrictions and increasing the persistent current (by having bigger junctions) to flux qubits containing SQUID junctions. For this we tried to measure changes in the qubits' transition line, as well as its T_1 and T_2.

We had a hard time optimizing the measurement but it payed off in the end. Qubit A was detected at 10 GHz at the optimal point and looks promising for SQUID-tuning. We are

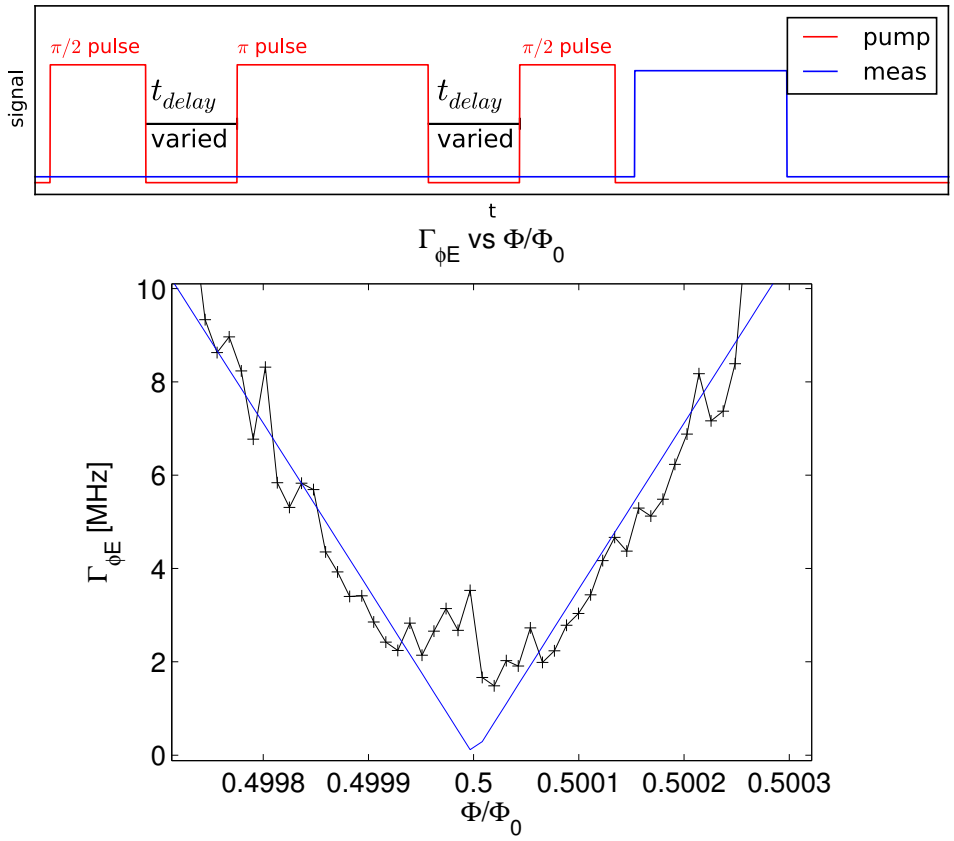

Figure 16: T_2 echo measurement sequence and results for flux qubit A showing the dependence of the pure echo dephasing rate as a function of the flux bias. A fit with a theoretical curve is shown and gives a flux noise of $8\mu\Phi_0/\sqrt{Hz}$ at 1 Hz. The deviation of the linear dependence in the vicinity of $\Phi_0/2$ may indicate the role of second order effects.

currently trying to characterize fully characterize qubit A at $^3/_2\Phi_0$, $^5/_2\Phi_0$, ...

Qubit B at the optimal point was too hot (1.2 GHz) to be measured directly without resorting to a dynamical cooling method like DDROP, something that we plan in the future. We did manage to measure its $T_1 \approx 1.5\mu s$ by placing ourselves off the optimal point (to bring it out of the hot regime). By looking at the dependence of the transition frequency on the magnetic field, we deduced that it has a large persistent current of $I_p^B \approx 800\,\mathrm{nA}$. This is exactly what we had hoped for by designing larger junctions.

Compared to[24], we also demonstrated the feasibility of using a e-beam to fabricate a 35-nm constriction[11]. This indicates that we now possess the first few necessary building blocks for coupling a single spin to a FQ in the future. The next step will be to work with 2D coplanar waveguide designs to introduce local flux lines which will allow a better and individual control on the flux qubits.

References

[1] N. Bar-Gill, L. M. Pham, A. Jarmola, D. Budker, and R. L. Walsworth. Solid-state electronic spin coherence time approaching one second. *Nature Communications*, 4:1743, 2013.

[2] P. Bertet, I. Chiorescu, G. Burkard, K. Semba, C. J. P. M. Harmans, D. P. DiVincenzo, and J. E. Mooij. Dephasing of a Superconducting Qubit Induced by Photon Noise. *Physical Review Letters*, 95(25):257002, 2005.

[3] Alexandre Blais, Ren-Shou Huang, Andreas Wallraff, S. M Girvin, and R. J Schoelkopf. Cavity quantum electrodynamics for superconducting electrical circuits: An architecture for quantum computation. *Physical Review A*, 69:62320, 2004.

[4] O. Buisson, F. Balestro, J. P. Pekola, and F. W. J. Hekking. One-Shot Quantum Measurement Using a Hysteretic dc SQUID. *Physical Review Letters*, 90(23):238304, 2003. Copyright (C) 2009 The American Physical Society; Please report any problems to prola@aps.org.

[5] I. Chiorescu, Y. Nakamura, C. J. P. M Harmans, and J. E Mooij. Coherent Quantum Dynamics of a Superconducting Flux Qubit. *Science*, 299(5614):1869–1871, March 2003.

[6] Pieter Christiaan. *Coupled Flux Qubits and Double Bifurcation Readout.* PhD thesis, 2010. TUDelft.

[7] M. H. Devoret, A. Wallraff, and J. M. Martinis. *Superconducting Qubits: A Short Review.* 2008.

[8] David P Divincenzo. The Physical Implementation of Quantum Computation. *Fortschritte der Physik*, 48:771–783, 2000.

[9] K. Geerlings, Z. Leghtas, I. M. Pop, S. Shankar, L. Frunzio, R. J. Schoelkopf, M. Mirrahimi, and M. H. Devoret. Demonstrating a Driven Reset Protocol for a Superconducting Qubit. *Phys. Rev. Lett.*, 110(12):120501, March 2013.

[11] unlike drawing an area in which the e-beam *scans* lines of pixels by going back and forth, the e-beam sweeps in 1 dimension rapidly the line.

[10] Lov K. Grover. A fast quantum mechanical algorithm for database search. pages 212–219, 1996.

[11] Ronald Hanson and David D. Awschalom. Coherent manipulation of single spins in semiconductors. *Nature*, 453(7198):1043–1049, June 2008.

[12] S. Haroche and J. M Raimond. *Exploring the quantum*. Oxford University Press, August 2006.

[13] G. Ithier, E. Collin, P. Joyez, P. J. Meeson, D. Vion, D. Esteve, F. Chiarello, A. Shnirman, Y. Makhlin, J. Schriefl, and G. Schön. Decoherence in a superconducting quantum bit circuit. *Physical Review B*, 72(13):134519, October 2005. Copyright (C) 2009 The American Physical Society; Please report any problems to prola@aps.org.

[14] Y. Kubo, F. R. Ong, P. Bertet, D. Vion, V. Jacques, D. Zheng, A. Dréau, J.-F. Roch, A. Auffeves, F. Jelezko, J. Wrachtrup, M. F. Barthe, P. Bergonzo, and D. Esteve. Strong Coupling of a Spin Ensemble to a Superconducting Resonator. *Physical Review Letters*, 105(14):140502, 2010.

[15] D. Marcos, M. Wubs, J. M. Taylor, R. Aguado, M. D. Lukin, and A. S. Sørensen. Coupling Nitrogen-Vacancy Centers in Diamond to Superconducting Flux Qubits. *Physical Review Letters*, 105(21):210501, November 2010.

[16] P. C. Maurer, G. Kucsko, C. Latta, L. Jiang, N. Y. Yao, S. D. Bennett, F. Pastawski, D. Hunger, N. Chisholm, M. Markham, D. J. Twitchen, J. I. Cirac, and M. D. Lukin. Room-Temperature Quantum Bit Memory Exceeding One Second. *Science*, 336(6086):1283–1286, 2012.

[17] T. P. Orlando, J. E. Mooij, Lin Tian, Caspar H. van der Wal, L. S. Levitov, Seth Lloyd, and J. J. Mazo. Superconducting persistent-current qubit. *Phys. Rev. B*, 60(22):15398–15413, December 1999.

[18] F. G. Paauw, A. Fedorov, C. J. P. M Harmans, and J. E. Mooij. Tuning the Gap of a Superconducting Flux Qubit. *Phys. Rev. Lett.*, 102(9):090501, March 2009.

[19] Hanhee Paik, D. I. Schuster, Lev S. Bishop, G. Kirchmair, G. Catelani, A. P. Sears, B. R. Johnson, M. J. Reagor, L. Frunzio, L. I. Glazman, S. M. Girvin, M. H. Devoret, and R. J. Schoelkopf. Observation of High Coherence in Josephson Junction Qubits Measured in a Three-Dimensional Circuit QED Architecture. *Phys. Rev. Lett.*, 107(24):240501, December 2011.

[20] A. Palacios-Laloy, F. Nguyen, F. Mallet, P. Bertet, D. Vion, and D. Esteve. Tunable Resonators for Quantum Circuits. *Journal of Low Temperature Physics*, 151(3):1034–1042, 2008.

[21] Agustin Palacios-Laloy. *Bits quantiques supraconducteurs et résonateurs : test de l'intégralité de Legget-Garg et lecture en un coup*. PhD thesis, 2010. Thèse de doctorat dirigée par Estève, Daniel Physique quantique Paris 6 2010.

[22] Wolfgang Pfaff, Tim H. Taminiau, Lucio Robledo, Hannes Bernien, Matthew Markham, Daniel J. Twitchen, and Ronald Hanson. Demonstration of entanglement-by-measurement of solid-state qubits. *Nat Phys*, 9(1):29–33, January 2013.

[23] Peter W. Shor. Polynomial-Time Algorithms for Prime Factorization and Discrete Logarithms on a Quantum Computer. *SIAM Journal on Computing*, 26(5):1484–1509, October 1997.

[24] M. Stern, G. Catelani, Y. Kubo, C. Grezes, A. Bienfait, D. Vion, D. Esteve, and P. Bertet. Flux Qubits with Long Coherence Times for Hybrid Quantum Circuits. *Phys. Rev. Lett.*, 113(12):123601, September 2014.

[25] J. Twamley and S. D. Barrett. Superconducting cavity bus for single nitrogen-vacancy defect centers in diamond. *Physical Review B*, 81(24):241202, 2010.

[26] Ze-Liang Xiang, Sahel Ashhab, J. Q. You, and Franco Nori. Hybrid quantum circuits: Superconducting circuits interacting with other quantum systems. *Rev. Mod. Phys.*, 85(2):623–653, April 2013.